



Unlocking the zinc isotope systematics of iron meteorites



L.J. Bridgestock^{a,*}, H. Williams^{b,c}, M. Rehkämper^{a,d,*}, F. Larner^{a,b}, M.D. Giscard^{a,d},
S. Hammond^e, B. Coles^a, R. Andreasen^a, B.J. Wood^b, K.J. Theis^f, C.L. Smith^d,
G.K. Benedix^g, M. Schönbachler^h

^a Department of Earth Science and Engineering, Imperial College London, SW7 2AZ, UK

^b Department of Earth Sciences, University of Oxford, OX1 3AN, UK

^c Department of Earth Sciences, Durham University, DH1 3LE, UK

^d Natural History Museum, London, SW7 5BD, UK

^e Centre for Earth, Planetary, Space & Astronomical Research, The Open University, Milton Keynes MK7 6BJ, UK

^f Dept. School of Earth, Atmospheric and Environmental Sciences, University of Manchester, M13 9PL, UK

^g Department of Applied Geology, Curtin University, Bentley, Western Australia, 6845, Australia

^h Institut für Geochemie und Petrologie, ETH Zürich, Clausiusstrasse 25, 8092 Zürich, Switzerland

ARTICLE INFO

Article history:

Received 20 March 2013

Received in revised form 16 May 2014

Accepted 19 May 2014

Available online 6 June 2014

Editor: T. Elliott

Keywords:

iron meteorites
stable isotopes
Zn isotopes
volatile elements
core formation

ABSTRACT

Zinc isotope compositions ($\delta^{66}\text{Zn}$) and concentrations were determined for metal samples of 15 iron meteorites across groups IAB, IIAB, and IIIAB. Also analyzed were troilite and other inclusions from the IAB iron Toluca. Furthermore, the first Zn isotope data are presented for metal–silicate partitioning experiments that were conducted at 1.5 GPa and 1650 K. Three partitioning experiments with run durations of between 10 and 60 min provide consistent Zn metal–silicate partition coefficients of ~ 0.7 and indicate that Zn isotope fractionation between molten metal and silicate is either small (at less than about $\pm 0.2\%$) or absent. Metals from the different iron meteorite groups display distinct ranges in Zn contents, with concentrations of 0.08–0.24 $\mu\text{g/g}$ for IIABs, 0.8–2.5 $\mu\text{g/g}$ for IIIABs, and 12–40 $\mu\text{g/g}$ for IABs. In contrast, all three groups show a similar range of $\delta^{66}\text{Zn}$ values (reported relative to 'JMC Lyon Zn') from $+0.5\%$ to $+3.0\%$, with no clear systematic differences between groups. However, distinct linear trends are defined by samples from each group in plots of $\delta^{66}\text{Zn}$ vs. $1/\text{Zn}$, and these correlations are supported by literature data. Based on the high Zn concentration and $\delta^{66}\text{Zn} \approx 0$ determined for a chromite-rich inclusion of Toluca, modeling is employed to demonstrate that the Zn trends are best explained by segregation of chromite from the metal phase. This process can account for the observed Zn– $\delta^{66}\text{Zn}$ –Cr systematics of iron meteorite metals, if Zn is highly compatible in chromite and Zn partitioning is accompanied by isotope fractionation with $\Delta^{66}\text{Zn}_{\text{chr-met}} \approx -1.5\%$. Based on these findings, it is likely that the parent bodies of the IAB complex, IIAB and IIIAB iron meteorites featured $\delta^{66}\text{Zn}$ values of about -1.0 to $+0.5\%$, similar to the Zn isotope composition inferred for the bulk silicate Earth and results obtained for chondritic meteorites. Together, this implies that most solar system bodies formed with similar bulk Zn isotope compositions despite large differences in Zn contents.

© 2014 Published by Elsevier B.V.

1. Introduction

Cosmochemical studies reveal a clear preference for compositional investigations of primitive and differentiated stony meteorites because their diverse elemental and isotopic chemistry is more readily exploited to examine early solar system conditions and processes. Iron meteorites, however, are also worthy of inves-

tigation, as they constitute the only accessible samples of planetary cores. Differentiated bodies are common in the solar system, and studies of irons are, therefore, important to advance our understanding of core formation and bulk planetary compositions.

Iron meteorites fall into the two categories of magmatic and non-magmatic irons. The former are considered to be core fragments from differentiated and subsequently disrupted asteroidal parent bodies. This conclusion is based on the observation of siderophile trace element trends, which can be explained by models of fractional crystallization of solid metal (e.g., Scott, 1972). Different groups of magmatic irons, distinguished by distinct trace element trends, mirror a range in redox conditions as well as cooling

* Corresponding authors at: Department of Earth Science and Engineering, Imperial College London, SW7 2AZ, UK. Tel.: +44 20 7594 6391.

E-mail address: markrehk@imperial.ac.uk (M. Rehkämper).

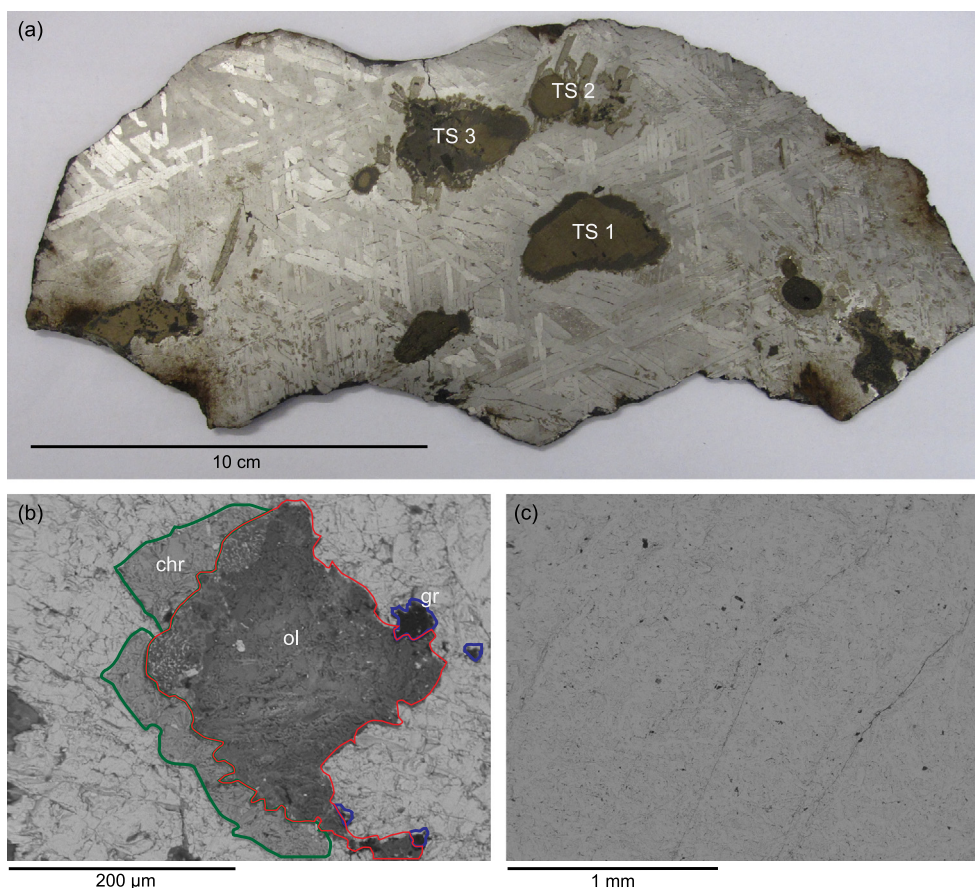


Fig. 1. Images of the Toluca (IAB) sample obtained for this study. Panel (a) shows a photograph of the entire Toluca IAB slab, indicating the positions of the three troilite nodules (TS1, TS2 and TS3) separated for analysis. Panel (b) shows a SEM electron backscatter image of an inclusion within TS3, with the main phases chromite (chr; green), graphite (gr; blue) and olivine (ol; red) highlighted in color. Panel (c) is an electron backscatter image of a fragment of TS1, showing graphite inclusions (as dark specs) within troilite. (For interpretation of the references to color in this figure, the reader is referred to the web version of this article.)

rates, indicating differences in starting composition and geochemical evolution (Mittlefehldt et al., 1998; Chabot and Haack, 2006; Benedix et al., 2013). In contrast, non-magmatic iron meteorites did not form as a single core in a differentiating asteroid. Possible models for their formation range from impact melting on the surface of an undifferentiated parent body (Choi et al., 1995; Wasson and Kallemeyn, 2002) to catastrophic impact, breakup and reassembly of a chondritic asteroid, which experienced partial metal–silicate differentiation (Benedix et al., 2000; Schulz et al., 2009; Theis et al., 2013).

Isotopic studies of iron meteorites are comparatively scarce because they are limited to analyses of siderophile and chalcophile elements (e.g., S, Mo, Ag, Os), which are sufficiently abundant in the metal to permit acquisition of precise data. Of more recent origin are stable isotope investigations of transition metals such as Fe, Ni and Cu (e.g., Zhu et al., 2001; Kehm et al., 2003; Luck et al., 2005; Moynier et al., 2007). Zinc isotopes are also potentially useful for the study of iron meteorites. Whilst only a very limited number of samples have been analyzed to date, the available results reveal significant Zn isotope variability (Luck et al., 2005; Moynier et al., 2007; Ghidan and Loss, 2011). More analyses are needed, however, before the isotopic data can be employed with confidence to constrain parent body processes and conditions.

The current study addresses this lack of data, through Zn isotope and concentration measurements for metal samples of 15 iron meteorites and analyses of inclusions from the group IAB iron Toluca. Further Zn data were obtained for samples from metal–silicate partitioning experiments that were conducted at 1.5 GPa and 1650 K. Together, these results were applied to (i) interro-

gate the processes responsible for the variable Zn contents and isotope compositions of iron meteorites and (ii) constrain the bulk Zn isotope compositions of the respective asteroid cores and parent bodies.

2. Samples and laboratory methods

2.1. Meteorite samples and sampling procedures

Metal samples of six group IIAB and six IIIAB iron meteorites were provided by the Natural History Museum, London, and obtained as solution aliquots of large samples (about 15 to 40 g; Table 1) that were digested for a companion study (Andreasen et al., 2012). For the IAB irons, an interior piece of Campo del Cielo and polished slabs of Toluca and Canyon Diablo were purchased from commercial vendors. Multiple pieces of metal were analyzed for Sikhote-Alin (IIAB) and the IAB irons Canyon Diablo and Toluca, to investigate small-scale heterogeneities in Zn isotope compositions and concentrations (Table 1).

Fragments of three troilite nodules were manually separated from the Toluca slab for additional analyses (Fig. 1). Inspection under reflected light revealed that the Toluca sulfide nodules TS1 and TS2 were composed of troilite with graphite rims, whilst TS3 contained a visible schreibersite exsolution and graphite inclusions within troilite. Fragments of TS1 and TS3 were further examined using scanning electron microscopy (SEM) at the Natural History Museum London (Fig. 1). This revealed that TS1 consisted of troilite with small inclusions of graphite and no other phases were observed. In contrast, TS3 featured troilite with abundant graphite

Table 1

Zinc isotope compositions, concentrations and further details for the iron meteorite samples analyzed in this study.

Sample	Group	Total sample (g) ^a	Mass for Zn analysis (g) ^b	Main phase(s)	$\delta^{66}\text{Zn}^c$	Zn conc. ^d ($\mu\text{g/g}$)	Mass fraction natural Zn	Cr ($\mu\text{g/g}$)
Campo del Cielo	IAB	5.70	0.011	Metal	2.09 ± 0.07	36.93 ± 0.18	0.98	8.39
Canyon Diablo 1 run 1 ^e	IAB	1.07	0.083	Metal	1.77 ± 0.10	27.52 ± 0.10	1.00	3.50
run 2 ^e		1.07	0.083		1.74 ± 0.09	27.53 ± 0.04	1.00	
Canyon Diablo 2 run 1 ^e	IAB	0.996	0.064	Metal	2.41 ± 0.07	19.44 ± 0.04	0.99	2.66
run 2 ^e		0.996	0.064		2.46 ± 0.09	19.44 ± 0.04	0.99	
Canyon Diablo 3	IAB	1.17	0.081	Metal	1.39 ± 0.10	32.38 ± 0.04	1.00	4.41
Toluca 1 run 1 ^e	IAB	7.02	0.034	Metal	2.50 ± 0.07	12.24 ± 0.06	0.98	4.85
run 2 ^e		7.02	0.034		2.45 ± 0.20	12.24 ± 0.06	0.98	
Toluca 2	IAB	10.8	0.024	Metal	1.66 ± 0.06	19.33 ± 0.08	0.99	5.33
TS1 Toluca sulfide inclusion 1	IAB	0.767	0.125	Troilite	2.4 ± 0.5	0.206 ± 0.016	0.77	
TS2 Toluca sulfide inclusion 2	IAB	0.583	0.059	Troilite	6.9 ± 1.2	0.242 ± 0.034	0.63	
TS3-D1 Toluca sulfide inclusion 3, 1st dissolution (HCl-HNO ₃ leach) ^f	IAB	0.299	0.021	Troilite, schreibersite	3.74 ± 0.17	9.52 ± 0.09	0.97	
TS3-D2 Toluca sulfide inclusion 3, 2nd dissolution (digestion of residue) ^f	IAB	0.036	0.005	Silicates, chromite	0.14 ± 0.06	154.4 ± 0.5	0.99	645
Chesterville	IIAB	16.8	0.280	Metal	1.63 ± 0.13	0.144 ± 0.007	0.85	
Coahuila	IIAB	31.0	0.201	Metal	1.47 ± 0.08	0.232 ± 0.010	0.86	
North Chile	IIAB	35.3	0.247	Metal	0.82 ± 0.10	0.239 ± 0.008	0.89	
San Francisco del Mezquital	IIAB	18.5	0.334	Metal	0.33 ± 0.11	0.080 ± 0.006	0.78	
Sikhote-Alin 1	IIAB	42.2	0.268	Metal	1.49 ± 0.12	0.151 ± 0.007	0.85	
Sikhote-Alin 2	IIAB	16.9	0.218	Metal	3.0 ± 0.4	0.088 ± 0.009	0.71	
Sikhote-Alin 3	IIAB	17.7	0.231	Metal	0.91 ± 0.14	0.214 ± 0.009	0.87	
Sikhote-Alin 4	IIAB	19.3	0.257	Metal	2.11 ± 0.17	0.122 ± 0.008	0.81	
Sikhote-Alin 5	IIAB	33.7	0.217	Metal	1.91 ± 0.17	0.129 ± 0.009	0.79	
Uwet	IIAB	17.0	0.224	Metal	1.35 ± 0.12	0.175 ± 0.009	0.84	
Bear Creek	IIIAB	17.1	0.303	Metal	1.69 ± 0.10	0.765 ± 0.007	0.97	
Boxhole	IIIAB	36.7	0.235	Metal	0.67 ± 0.10	1.594 ± 0.008	0.98	
Carthage	IIIAB	17.4	0.308	Metal	0.75 ± 0.10	1.624 ± 0.007	0.99	
Charcas	IIIAB	18.6	0.232	Metal	1.12 ± 0.10	1.800 ± 0.010	0.98	
Henbury	IIIAB	34.5	0.177	Metal	1.04 ± 0.10	2.529 ± 0.011	0.98	
Thunda	IIIAB	33.3	0.214	Metal	1.77 ± 0.10	0.822 ± 0.009	0.96	
USGS BCR-2	(SRM)			(basalt)	$+0.25 \pm 0.10$			
Published data BCR-2 ^g					$+0.23$ to $+0.33$			
USGS BHVO-2	(SRM)			(basalt)	$+0.40 \pm 0.10$			
Published data BHVO-2 ^g					$+0.17$ to $+0.48$			
USGS NOD-P-1/sample A	(SRM)			(Fe-Mn nodule)	$+0.78 \pm 0.10$			
USGS NOD-P-1/sample B	(SRM)			(Fe-Mn nodule)	$+0.81 \pm 0.10$			
USGS NOD-P-1/sample C	(SRM)			(Fe-Mn nodule)	$+0.77 \pm 0.10$			
Published data NOD-P-1 ^g					$+0.55$ to $+0.87$			

^a Total mass of meteorite that was dissolved in the laboratory for Zn isotope and other analyses.^b Meteorite mass that corresponds to the meteorite solution aliquot, which was processed for Zn isotope analysis.^c The $\delta^{66}\text{Zn}$ data are reported relative to the JMC Lyon Zn isotope reference material (Maréchal et al., 1999). The quoted uncertainties ($\pm 2\text{sd}$) reflect both the mass spectrometric reproducibility and the uncertainty of the blank correction (see supplementary text).^d The uncertainty of Zn concentrations ($\pm 2\text{sd}$) reflects both the mass spectrometric reproducibility and the uncertainty of the blank correction (see supplementary text).^e Run 1 and run 2 denote duplicate analyses of the same sample solutions.^f Sample TS3-D1 was produced by partial dissolution/leaching of Toluca sulfide nodule 3 (TS3) with HCl-HNO₃ (see text). Sample TS3-D2 was produced by digestion of the insoluble residue remaining after partial dissolution of the nodule with HCl-HNO₃. The TS3-D1 and TS3-D2 sample weights were determined after drying of the respective solutions on a hotplate.^g The published reference data for the SRMs are from Jochum et al. (2005).

Table 2

Experimental conditions of the partitioning experiments, Zn concentrations and isotope compositions of the run products, and Zn distribution coefficients and isotope fractionations determined from these.

	Zn-doped silicate ^a	Experiment A170	Experiment B101	Experiment B96	Experiment B99
Capsule material	–	silica	MgO	MgO	MgO
Run time (min)	–	60	10	30	60
Silicate [Zn] (μg/g)	54.0	23.7	155	101	166
Metal [Zn] (μg/g)	–	59.9	111	76.8	100
δ ⁶⁶ Zn silicate	–0.46 ± 0.05	+0.12 ± 0.08	+0.57 ± 0.11	+0.67 ± 0.07	+0.65 ± 0.11
δ ⁶⁶ Zn metal	–	+0.09 ± 0.19	+0.71 ± 0.02	+0.46 ± 0.13	+0.68 ± 0.14
D _{met-sil} ^b	–	2.5	0.71	0.76	0.60
Δ ⁶⁶ Zn _{met-sil} ^c	–	–0.03 ± 0.21	+0.14 ± 0.11	–0.21 ± 0.15	+0.03 ± 0.18

The δ⁶⁶Zn data are reported relative to the Lyon Zn isotope reference material (Maréchal et al., 1999). The quoted uncertainties denote the 2sd reproducibility calculated from 2 or 3 individual runs of the samples. For sample A170 metal, which was only analyzed once, the uncertainty is based on the reproducibility (±2sd) obtained for bracketing runs of a matching standard solution. The Zn concentration data have an uncertainty of better than ±1% (2sd).

^a Composition of the silicate material including added Zn that was employed in the metal–silicate partitioning experiments.

^b $D_{\text{met-sil}} = [\text{Zn}]_{\text{met}}/[\text{Zn}]_{\text{sil}}$.

^c $\Delta^{66}\text{Zn}_{\text{met-sil}} = \delta^{66}\text{Zn}_{\text{met}} - \delta^{66}\text{Zn}_{\text{sil}}$.

and silicate inclusions, consisting predominantly of olivine with some pyroxene and plagioclase, and minor proportions (~1%) of chromite and schreibersite.

2.2. Experimental petrology techniques

The starting materials were prepared from high purity oxide and metal powders to provide a mix of about 30% Fe metal and 70% silicate, the latter approximating the 1.5 GPa eutectic composition of the system anorthite–diopside–forsterite (An₅₀Di₂₈Fo₂₂; Presnall et al., 1978). The silicate starting material was doped with 2 wt% each of Zn (as ZnO) and Fe (as FeO). Prior to use, the powder mixtures were ground three times under acetone and subsequently dried, to ensure a homogeneous, fine-grained starting material.

All experiments were performed at 1.5 GPa in an end-loaded piston cylinder apparatus at the Department of Earth Sciences, University of Oxford, using a ½-inch pyrophyllite–SiO₂ glass assembly with a graphite heater. The internal spacers consisted of MgO that had been fired at 1000 °C. Both MgO and SiO₂ glass capsules were used (Table 2). Temperatures were measured using W₉₅Re₅–W₇₄Re₂₆ thermocouples, with a temperature of 1650 °C chosen to ensure melting of both the silicate and metal portions of the charges. Experimental run times ranged from 10 to 60 min (Table 2), in order to assess the effects of run duration on the extent of Zn loss from the charges and the isotopic fractionation between metal and silicate.

On completion, the experiments were quenched by turning off power to the heaters whilst maintaining run pressure, which was subsequently slowly released. The charges were then lightly crushed to break open the capsules and expose the run products, which consisted of a homogeneous, quenched silicate glass and iron metal. In the recovered experiments, the metal segregated into one large (>300 μm diameter) globule surrounded by homogeneous silicate glass. The experimental products were lightly crushed under ethanol to separate the metal globule and silicate fragments, which were handpicked for analysis under a binocular microscope.

2.3. Leaching and digestion of samples

To remove surface contamination, all meteorite samples were sequentially leached at room temperature with (i) 0.5 M HBr (1 h, ultrasonic bath), (ii) 6 M HCl (1 h, ultrasonic bath) and (iii) aqua regia (30 min) with intermittent rinses in 18 MΩcm H₂O. Following leaching, which removed about 20 to 30% of the original meteorite mass, the samples were digested in aqua regia at 80 °C on a hotplate. The digestion of the sulfide nodules was incomplete and the insoluble residue was removed by centrifugation. Troilite,

and schreibersite for TS3, were observed to dissolve in this first digestion step. The insoluble residue of TS3, presumably comprising silicates and chromite, was dissolved in a second step to yield sample TS3-D2. This involved (i) treatment with a 3 + 1 mixture of 28 M HF + 15.4 M HNO₃ at 80 °C on a hotplate for 1 week, (ii) evaporation to dryness and digestion in 6 M HCl at 80 °C on a hotplate for 2 days, and (iii) evaporation to dryness and digestion in aqua regia in a Parr bomb at 120 °C for 2 days. Finally, all samples were dissolved in 6 M HCl for aliquoting.

The separated silicate glass and metal fractions from the high-pressure experiments were also cleaned prior to digestion, by treating with ethanol in an ultrasonic bath (20 min); to remove residual organics) followed by 18 MΩcm H₂O (20 min). The samples were then digested using an 8 + 1 mixture of 28 M HF + 15.4 M HNO₃ (silicates) or aqua regia (metal) at 130 °C and finally dissolved in 6 M HCl for aliquoting.

2.4. Sample preparation and mass spectrometric analyses

The Zn isotope measurements were carried out at the Imperial College MAGIC Laboratories using procedures modified from Arnold et al. (2010). Only a brief outline of the methods is presented here, with further details available in the supplementary material. Aliquots of the sample solutions were first equilibrated with an appropriate volume of a ⁶⁴Zn–⁶⁷Zn double spike and Zn was then separated from the sample matrix by ion exchange chromatography (Arnold et al., 2010). The isotopic analyses were performed with a Nu Plasma HR MC-ICP-MS instrument using a desolvation system for sample introduction. The analyses utilized Zn solutions with concentrations of 40 to 60 ng/ml in 0.1 M HNO₃ at instrumental sensitivities for Zn of ~110 V (μg/ml)^{–1}.

The instrumental mass bias encountered in the measurements was corrected using double spike methods adapted from Arnold et al. (2010), whereby corrections for spectral interferences from ⁶⁴Ni⁺ and Ba²⁺ ions were also subjected to a mass bias correction. The Zn isotope compositions of the samples were determined relative to matching standard solutions that were prepared as mixtures of our in-house “London Zn” standard with the Zn double spike. Isotopic differences between samples and standards are reported as δ⁶⁶Zn, calculated from the ⁶⁶Zn/⁶⁴Zn ratio (R):

$$\delta^{66}\text{Zn} = [(R_{\text{Sample}}/R_{\text{Standard}}) - 1] \times 1000 \quad (1)$$

In the following, δ⁶⁶Zn is reported relative to the JMC Lyon Zn reference solution (Maréchal et al., 1999). To this end, the results were corrected for an isotopic offset of δ⁶⁶Zn = +0.12 ± 0.04‰ for London Zn relative to Lyon Zn (Larner and Rehkämper, 2012; Arnold et al., 2010). The Zn concentrations of the samples were determined by isotope dilution using the ⁶⁷Zn/⁶⁸Zn ratios measured in the double spike runs.

The Zn concentration and isotope data shown in Table 1 are corrected for laboratory blank and the reported uncertainties propagate the errors of both the blank correction and the mass spectrometric reproducibility (see supplementary text and Table S1). Four analyses yielded a total procedural Zn blank of 5 ± 2 ng (total range). With this, the blank corrections were small or insignificant for the majority of the samples but important for the Zn-depleted IIAB irons and nodules TS1, TS2 (Table 1). The samples from the partitioning experiments featured sufficient Zn (>150 μg) such that blank corrections were negligible and not applied. The mass spectrometric uncertainty for the $\delta^{66}\text{Zn}$ measurements (typically about $\pm 0.1\%$, 2sd), are generally based on the reproducibility obtained for multiple runs of matching London Zn–Zn double spike solutions (see supplementary text). This procedure is justified by results obtained for replicate analyses of (i) Toluca 1, conducted within the same measurement session and (ii) Canyon Diablo 1 and 2, carried out on different days with different sample introduction systems. In all cases, these analyses yielded $\delta^{66}\text{Zn}$ values that are identical to within $\pm 0.05\%$ or better (Table 1).

There are no suitable geological standard reference materials (SRMs) to document the quality of our Zn isotope analyses for iron meteorites. In the absence of such materials, measurements were carried out for alternative SRMs for which published $\delta^{66}\text{Zn}$ data are available – a metal-rich ferromanganese (Fe–Mn) nodule and two basalts. In all cases, these analyses yielded results that are in excellent agreement with published reference values (Table 1).

Additional concentration analyses for Cr and other elements were carried out for the metal samples of the IAB irons and Toluca inclusion TS3–D2 (Table 1, supplementary Table S2). These measurements were performed at the Open University by quadrupole ICP–MS (see supplementary text for details).

3. Results and discussion

3.1. Samples from petrological experiments – isotope fractionation during metal–silicate partitioning

A single run of 60 min was carried out in a silica capsule (experiment A170), whilst a series of experiments with durations of 10 min (B101), 30 min (B96), and 60 min (B99) were performed in MgO capsules (Table 2). Subsequent analyses provided both Zn isotope and concentration data, that were used to calculate Zn metal–silicate distribution coefficients ($D_{\text{met-sil}} = [\text{Zn}]_{\text{met}}/[\text{Zn}]_{\text{sil}}$) and isotope fractionations $\Delta\delta^{66}\text{Zn}_{\text{met-sil}} = \delta^{66}\text{Zn}_{\text{met}} - \delta^{66}\text{Zn}_{\text{sil}}$ (Table 2).

The $D_{\text{met-sil}}$ values for the MgO capsule experiments are remarkably consistent at 0.60 to 0.76 (Table 2), in agreement with results from previous high-pressure experimental studies (Corgne et al., 2008; Lagos et al., 2008; Mann et al., 2009). The consistency of the $D_{\text{met-sil}}$ values obtained for run durations ranging from 10 to 60 min provides strong evidence for the attainment of Zn equilibrium between metal and silicate during the experiments. A higher value of $D_{\text{met-sil}} \approx 2.5$ was obtained for the silica capsule experiment A170 (Table 2), and this presumably reflects the known effects of melt polymerization on Zn partitioning into silicate melts (Kohn and Schofield, 1994). Here, reaction of the SiO_2 capsule with the experiment may have raised the Si content of the melt, thereby increasing the degree of melt polymerization. The stability of Zn in silicate melts appears to decrease with increasing degree of polymerization and this raises the effective metal–silicate Zn partition coefficient at high Si contents.

In terms of Zn isotope partitioning, the metal and silicate phases of all experimental runs, irrespective of capsule type, display higher $\delta^{66}\text{Zn}$ values than the starting material (with $\delta^{66}\text{Zn} = -0.46 \pm 0.05$), but the effect is most extreme for the MgO experiments (Table 2). We speculate that this reflects preferential loss

of isotopically light Zn from the experimental charges during the runs. The Zn loss is more pronounced for the MgO capsules, presumably due to the more porous nature of polycrystalline MgO relative to silica glass. This initially appears counterintuitive, as the Zn concentrations determined for the metal and silicate fractions of the MgO experiments are higher than for the silica capsule experiment A170. However, the observed effects can be explained by progressive dissolution of the silica capsule, which results in a larger volume for the A170 experiment and therefore Zn dilution. The dilution effect is particularly apparent in the low Zn concentration determined for the silicate phase extracted from A170. Unfortunately, it was not possible to quantify the extent of Zn loss from the experimental charges, as the silicate glass could not be fully recovered from any of the experiments.

The Zn metal–silicate isotope fractionation $\Delta\delta^{66}\text{Zn}_{\text{met-sil}}$ ranges from -0.14 ± 0.12 (MgO capsule, 10 min) to $+0.21 \pm 0.15$ (MgO capsule, 30 min), whereby the silica capsule experiment A170 (60 min) features $\Delta\delta^{66}\text{Zn}_{\text{met-sil}} = +0.04 \pm 0.21$. Significantly, the time series experiments conducted in MgO capsules show no systematic correlation for the magnitude or direction of the metal–silicate fractionation with run time. This probably reflects that the isotopic differences between metal and silicate are small (at $\leq 0.21\%$) relative to the analytical uncertainties and the larger isotopic effects that are generated by Zn loss from the capsules. In addition, the two 60 min experiments A170 (silica capsule) and B99 (MgO capsule) both display $\Delta\delta^{66}\text{Zn}_{\text{met-sil}}$ values that are within uncertainty of $\pm 0\%$ (Table 2). Taken together, these observations suggest that compositional and isotopic equilibrium are closely approached or established within 60 min. Furthermore, they indicate that Zn isotope fractionation between molten metal and silicate is either small or absent at the conditions of the experiments.

To place our findings into context, the 1.5 GPa pressure of our experiments corresponds to a depth of ~ 45 km on Earth, whilst metal segregation and core formation on even the largest asteroids will have occurred at ≤ 0.2 GPa (McCoy et al., 2006). This relatively small pressure difference should have little effect on isotopic fractionations (Criss, 1999), a conclusion confirmed by preliminary Pt–wire metal–silicate segregation experiments, conducted at 1000°C and atmospheric pressure (Moynier et al., 2005), which yielded $\Delta\delta^{66}\text{Zn}_{\text{met-sil}} \approx -0.1\%$. We conclude that, within the investigated pressure range, which is directly applicable to iron meteorite parent bodies, there is no substantial Zn isotope fractionation during metal–silicate partitioning. Given the absence of any significant relationship between pressure and the magnitude of observed Zn stable isotope effects, this conclusion is also tentatively accepted as applicable to the Earth. Further experiments at higher pressures and temperatures are required to confirm this, however.

3.2. Zn concentrations and isotope compositions of the iron meteorites

The Zn concentrations of the iron meteorite metal samples vary by nearly a factor of 500 from about 0.08 $\mu\text{g/g}$ (for a IIAB iron) to more than 35 $\mu\text{g/g}$ (for a IAB; Fig. 2a, Table 1). The highest Zn abundance of ~ 150 $\mu\text{g/g}$ was determined for TS3–D2, which represents the silicate and chromite phases of TS3, whilst the Toluca troilite nodules TS1 and TS2 are depleted in Zn (at ~ 20 $\mu\text{g/g}$) relative to the metal. Metals from each iron meteorite group display a distinct range of Zn concentrations, of about 0.08 to 0.24 $\mu\text{g/g}$ for IIABs, 0.75 to 2.5 $\mu\text{g/g}$ for IIIABs, and 12 to 37 $\mu\text{g/g}$ for the IAB irons (Fig. 2, Table 1), and these ranges are in good agreement with published Zn data, with the exception of a few outliers that may reflect Zn contamination (Fig. 2a). Notably, the non-magmatic IAB and IIICD irons display overlapping Zn contents, in accord with the previous conclusion that these two groups are closely related (Wasson and Kallemeyn, 2002). Samples of both groups are therefore designated as IAB complex irons in the following.

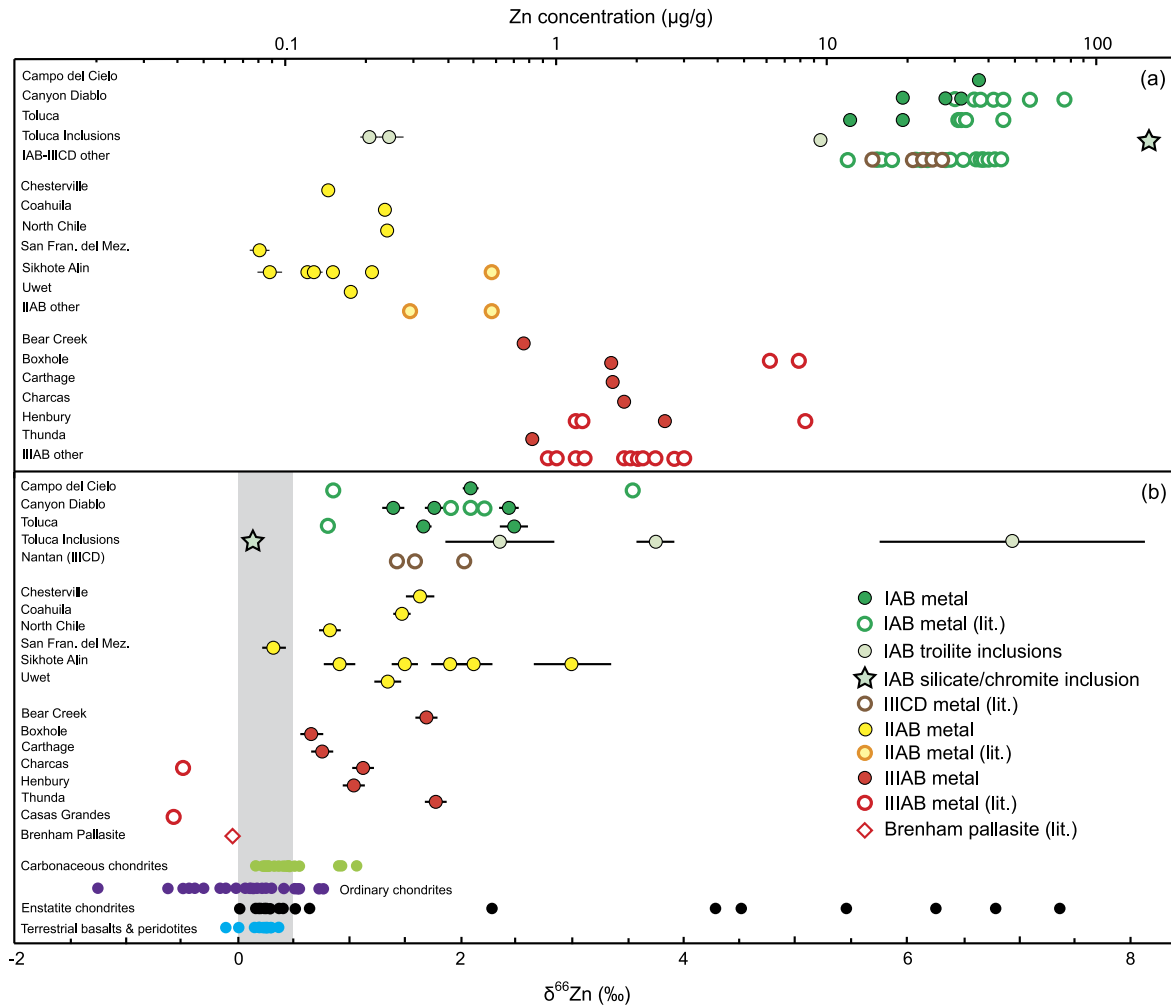


Fig. 2. Shown are (a) Zn concentrations and (b) Zn isotope compositions (as $\delta^{66}\text{Zn}$) of iron meteorite metal samples and inclusions. Both panels feature the results of the present study and iron meteorite data from the literature (lit.). Also shown in (b) are published $\delta^{66}\text{Zn}$ values for terrestrial mantle-derived basalts/peridotites as well as carbonaceous, ordinary and enstatite chondrites. The gray shaded field denotes the suggested Zn isotope composition of the bulk silicate Earth with $\delta^{66}\text{Zn} = +0.25 \pm 0.25\%$. The literature data and sources are compiled in supplementary Tables S3, S4, S7 and S8.

The $\delta^{66}\text{Zn}$ values of the iron meteorite metals range from $+0.33\%$ to $+3.0\%$, whilst the Toluca inclusions display more extreme isotope compositions with $\delta^{66}\text{Zn}$ as low as $+0.14 \pm 0.06\%$ (for silicate–chromite sample TS3-D2) and as high as $+6.9 \pm 1.2$ (for troilite nodule TS2; Fig. 2b, Table 1). In contrast to the concentration data, the isotopic results for the metal samples reveal no clear systematic differences between the iron meteorite groups. This conclusion is reinforced when our $\delta^{66}\text{Zn}$ values are combined with sparse published Zn isotope data for irons (Fig. 2b). In detail, this combined dataset provides average $\delta^{66}\text{Zn}$ values of $+1.9 \pm 0.5\%$, $+1.5 \pm 0.7\%$ and $+0.7 \pm 0.8\%$ for the IAB complex, IIAB and IIIAB groups, respectively (supplementary Table S3; uncertainties are $\pm 1\text{sd}$).

Of further interest is that variable Zn compositions were determined for multiple pieces of metal from Sikhote–Alin and this variability is confirmed by replicate analyses of metal samples from Canyon Diablo and Toluca (Fig. 2, Table 1). Furthermore, the ranges of Zn concentrations and $\delta^{66}\text{Zn}$ values recorded by the sub-samples of these three meteorites span nearly the entire ranges observed for the respective iron meteorite groups. In particular, the five Sikhote–Alin metals show a concentration range of 0.088 to 0.214 µg/g and a range of $\delta^{66}\text{Zn}$ from $+0.91$ to $+3.0$, compared with 0.080–0.239 µg/g and $\delta^{66}\text{Zn}$ of $+0.33$ to $+3.0$ for the entire IIAB group.

Within each iron meteorite group, the Zn concentrations and isotope compositions of the metals display a distinct negative correlation, albeit with significant scatter (Fig. 3), and even more convincing correlations are obtained in plots of $\delta^{66}\text{Zn}$ values versus $1/[\text{Zn}]$ (Figs. 4a–c). In addition, the IAB and IIIAB trends are reinforced by literature results for further samples of these groups and published data for Brenham pallasite metal extends the IIIAB trend (Figs. 3, 4), in agreement with the suggestion that pallasites and IIIAB irons are from the same parent body (Scott, 1977).

3.3. Elemental and isotopic fractionation of Zn within iron meteorite groups – origin of the $\delta^{66}\text{Zn}$ vs. Zn trends

Most terrestrial mantle-derived rocks display a limited range of $\delta^{66}\text{Zn}$ values between about ± 0 and $+0.5\%$ (Fig. 2b). In comparison, the majority of iron meteorite metals have significantly higher $\delta^{66}\text{Zn}$ (Figs. 2b, 3). However, the observed $\delta^{66}\text{Zn}$ vs. $[\text{Zn}]$ trends for the three iron groups extend toward and even overlap with terrestrial Zn isotope compositions at high Zn contents (Fig. 2b). It is therefore possible that the correlations reflect variable contamination of iron meteorite metal samples with high indigenous $\delta^{66}\text{Zn}$ by terrestrial Zn, which features $\delta^{66}\text{Zn} \approx 0\%$. Whilst this is an unlikely scenario, as all samples were extensively leached prior to digestion, it is nonetheless conceivable because (i) Zn is an ubiquitous anthropogenic contaminant (similar to Pb) and (ii) previous

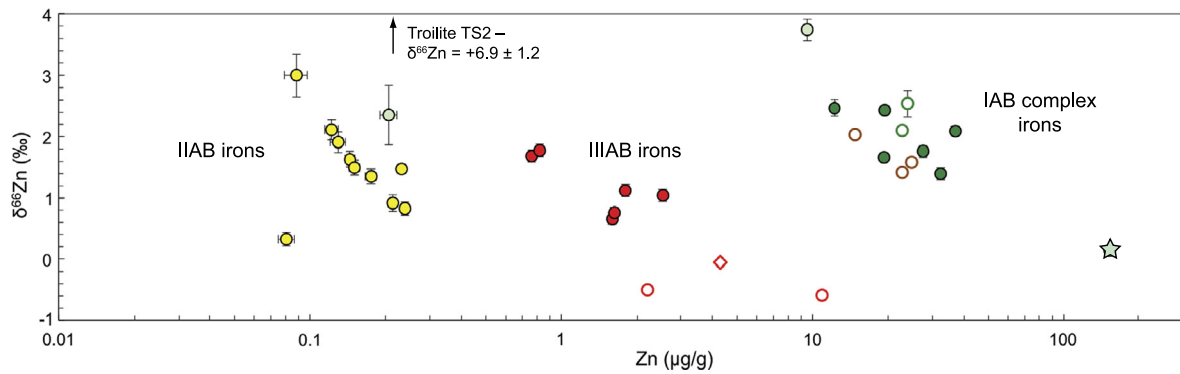


Fig. 3. Plot of $\delta^{66}\text{Zn}$ vs. Zn concentration for the samples analyzed in this study and iron meteorite data from the literature. Together, the results highlight the three distinct trends defined by IAB complex, IIAB, and IIIAB irons. The symbols are as defined in Fig. 2 and the uncertainties are shown as listed in Table 1 or the original publications. Literature data and sources are compiled in supplementary Table S3.

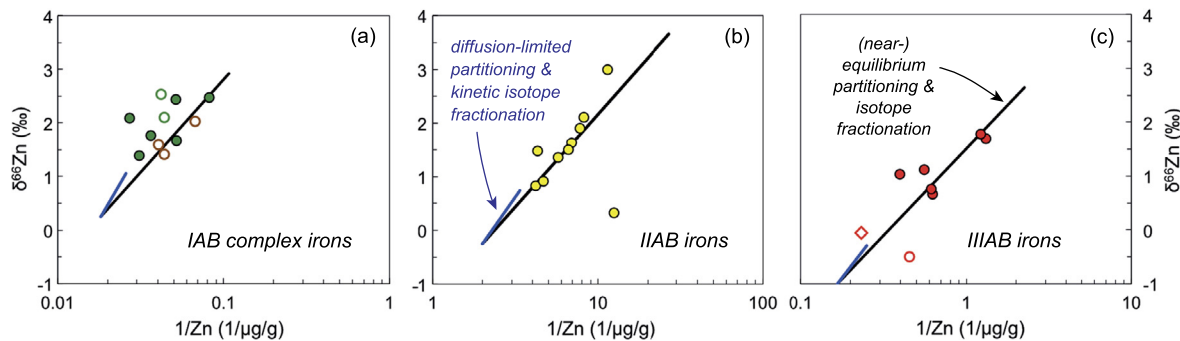


Fig. 4. Plots of $\delta^{66}\text{Zn}$ vs. $1/\text{Zn}$ concentration for (a) IAB complex, (b) IIAB, and (c) IIIAB iron meteorites, with data from this study and the literature. The symbols are as defined in Fig. 2. Each dataset is in accord with a distinct trend. The bold lines display the results of the chromite segregation model of Table 3, with the two endmember cases of (1) equilibrium partitioning and isotope fractionation of Zn (black lines) and (2) diffusion-limited partitioning and kinetic isotope fractionation for Zn (blue lines). Note that the equilibrium trends are 'longer' because they are associated with much larger Zn distribution coefficients $D_{\text{chr-met}}$ than the 'kinetic trends' (Table 3). Literature data and sources are given in supplementary Table S3. Uncertainties are not shown for simplicity and the data for Casas Grandes IIIAB, with an anomalously high Zn content of 10.9 $\mu\text{g/g}$ (Luck et al., 2005) that may reflect contamination, is omitted from panel (c). (For interpretation of the references to color in this figure, the reader is referred to the web version of this article.)

work has shown that it is difficult to release Pb contamination from iron meteorites even during prolonged leaching (Göpel et al., 1985; Nielsen et al., 2006). However, for each meteorite sample the same very specific conditions of contamination by terrestrial Zn and mixing with indigenous meteoritic Zn would be required, to generate the distinct trends defined by the three iron meteorite groups. A more likely consequence of terrestrial Zn contamination would be to create scatter in the data and obviate any previous systematic relationships. The Zn correlations of the samples (Figs. 3, 4a–c) are hence most plausibly explained by indigenous processes, which occurred on the meteorite parent bodies. Such processes are discussed and evaluated below.

A key observation is that the variability of Zn concentrations and isotope compositions between different metal samples of the same meteorite (Canyon Diablo, Toluca, Sikhote-Alin) is of a similar magnitude as the variability observed between metals from different irons belonging to the same group. This finding stands in contrast to the systematic siderophile element trends of magmatic irons that are explained by models of metal crystallization. Namely, the latter models predict elemental variations of a much lower magnitude in individual meteorites compared to those displayed by the entire group (e.g., Wasson, 1999). A similar inference can be made for the IAB metal samples of this study, as these exhibit strong siderophile element correlations that are in agreement with published trends (which are explained by melting and batch metal crystallization models) but there are no correlations between siderophile elements and either Zn concentrations or isotope compositions (see supplementary Table S2). Taken together, this implies that the observed Zn systematics (Figs. 3, 4a–c) are not

a consequence of metal crystallization but generated by distinct processes. These processes must operate on a relatively small (cm- to m-scale) to produce the variable Zn contents and $\delta^{66}\text{Zn}$ values determined for different samples of the same meteorite (Fig. 2).

In the following, alternative interpretations for the Zn trends (Figs. 3, 4a–c) are assessed, which call on the partitioning of Zn into minor, non-metal phases, most likely troilite, silicates and/or chromite. The available data (Table 1 and Luck et al., 2005) show that troilite typically features lower Zn contents than coexisting metal. As troilite is a common but generally minor phase in irons (Buchwald, 1977), partitioning of Zn into sulfide nodules is unlikely to have a significant impact on the overall Zn systematics of iron meteorites. The high Zn concentration ($\sim 150 \mu\text{g/g}$) and low $\delta^{66}\text{Zn}$ (of $+0.14\text{‰}$) determined for sample TS3-D2, which was produced by dissolution of silicate and chromite material associated with troilite nodule TS3 (Fig. 1), suggests that one or both of the former phases is responsible for the elemental and isotopic variations of Zn in the iron meteorites studied here. Notably, the presence of chromite within sample TS3-D2 is confirmed by the high Cr content of $645 \mu\text{g/g}$ (Table 1).

Silicate inclusions featuring olivine, pyroxene, and plagioclase are commonly observed in non-magmatic irons but are extremely rare in IIAB and IIIAB irons (Haack and McCoy, 2003). Such minerals typically feature Zn contents of only about 10 to $200 \mu\text{g/g}$ (Mittlefehldt et al., 1998). Therefore, sequestration of isotopically light Zn (e.g., $\delta^{66}\text{Zn} \approx 0$) into silicates is unlikely to generate the Zn trends of Figs. 3, 4a–c. This is further supported by our (and previous) partitioning experiments, which show that Zn is only moderately enriched in silicates compared to Fe metal

($D_{\text{met-sil}} \approx 0.7$; Table 2). Chromite, in contrast, is a minor but common accessory phase in IAB complex, IIAB and IIIAB irons (e.g., Buchwald, 1977; Mittlefehldt et al., 1998). The mineral plays a key role in controlling the abundance of Cr in the metal phase of irons and variable ZnO contents of $\leq 0.02\%$ to $>2\%$ are reported for chromite inclusion, thereby rendering this phase as the (or one of the) most important host(s) of Zn in iron meteorites (Bunch et al., 1970; Buchwald, 1977; Kracher, 1985; Wasson et al., 1999).

3.4. Modeling of the Zn trends based on chromite formation and segregation

In the following, modeling is applied to investigate whether partitioning of Zn into chromite, which segregates from the metal during cooling, can indeed account for the distinct Zn trends of the three iron meteorite groups (Figs. 3, 4a–c). The Cr concentrations are explicitly considered in the modeling and compared with the Cr contents of iron meteorites, as determined either in this study (on aliquots of the IAB irons; Table 1) or in previous investigations (supplementary Tables S4, S5). In detail, forward modeling is applied to identify reasonable upper and lower bounds for the key parameters of ‘chromite segregation’ models (Table 3), which produce good fits to the observed Zn– $\delta^{66}\text{Zn}$ –Cr systematics (Figs. 4, 5). The characteristics of these models are discussed below.

For the magmatic IIAB and IIIAB irons, the modeling uses initial Cr concentrations for the metal $[\text{Cr}]_{\text{met-0}}$ of 350 $\mu\text{g/g}$ (Table 3), in accord with published data (Kracher, 1983; Wasson et al., 1999; Chabot et al., 2009). No direct constraints on $[\text{Cr}]_{\text{met-0}}$ are available for the IAB irons. Our preferred value of 300 $\mu\text{g/g}$ provides a good fit to the data and is based on the assumption that different iron groups should feature similar $[\text{Cr}]_{\text{met-0}}$.

Chromite segregation is modeled until the Cr concentration of the metal is reduced to 5 $\mu\text{g/g}$, in agreement with the low Cr contents observed in this study and previous investigations (Fig. 5). We note that the Cr abundances determined here for the IABs are generally lower in comparison to literature Cr data for IAB complex irons and most published results for IIABs and IIIABs (Fig. 5). Based on this difference, it could be argued that the literature Cr data, acquired by neutron activation (INAA) on solid samples, are not suitable for evaluating the proposed chromite segregation model, as the high Cr contents reflect INAA detection of Cr both in residual metal and in dispersed chromite grains, which segregated from the former. In contrast, our solution-based analyses may yield lower Cr abundances because chromite grains are not dissolved when the metal samples are digested by hotplate treatment only.

Some key observations indicate, however, that the literature Cr data are nonetheless suitable for constraining the chromite segregation model. (i) Both our and the published IAB Cr results show similar systematics (Fig. 5a, d) in that Zn concentrations and $\delta^{66}\text{Zn}$ are variable at a given Cr abundance. (ii) Published Cr abundances for IIAB and IIIAB irons show a trend of decreasing Cr with increasing Ni concentration even though Cr is expected to display incompatible behavior during metal crystallization, and thus higher concentrations with increasing Ni. The observed systematics are interpreted to reflect depletion of Cr in residual metal as a result of chromite segregation, and where chromite is typically not sampled when metal samples of irons are prepared for analysis (Wasson et al., 1999; Chabot et al., 2009). This indicates the variable Cr abundances of irons determined both in this and earlier studies are primarily a consequence of chromite segregation from metal with high initial Cr contents.

Given the above conclusion, the observed difference in the IAB Cr abundances determined here and previously most reasonably reflects (i) small-scale sample heterogeneities, (ii) the presence of minor chromite within the metal samples, which contributes to the Cr budget of the INAA measurements but not our solution-based

analyses, and/or (iii) dispersed residual Cr in the metal, which is hosted in micro-inclusions (e.g., carlsbergite, CrN; Wasson et al., 1999) that are not fully digested during the metal dissolution procedure. Considering that all available Cr data for IAB complex, IIAB and IIIAB irons show similar minimum Cr abundances of about 5 to 30 $\mu\text{g/g}$, it is reasonable to conclude the lowest residual Cr contents for the metal phase of all three groups is about 10 $\mu\text{g/g}$ or less, in accord with the assumptions of the chromite segregation model (Fig. 5).

The range of Zn contents and isotope compositions observed at low (≤ 50 $\mu\text{g/g}$) Cr concentrations for all three groups of irons (Fig. 5) requires that the models apply variable Zn metal–chromite partition coefficients $D_{\text{chr-met}}$ and isotope fractionation factors $\alpha_{\text{chr-met}}$ (Table 3). In detail, good fits to the Zn–Cr systematics of all three groups are obtained using similar maximum and minimum $D_{\text{chr-met}}$ values of 2800–3500 and 550–700, respectively (Table 3). Similarly, fitting of the models yields consistent ranges for $\alpha_{\text{chr-met}}$, of between 0.9977 and 0.9985 for the IAB complex irons and of between 0.9981 and 0.9986 for IIAB, IIIAB iron meteorites (Table 3).

Such variable elemental and isotopic partitioning behavior (as inferred by the modeling) is feasible but only realistic if it can be related to physical or chemical changes in the partitioning system. Thus it is significant that previous studies concluded that chromite formation takes place over a large range of temperatures and conditions in iron meteorite parent bodies. In detail, it has been suggested that formation and growth of chromite occurs both as an early liquidus phase during metal crystallization (Kracher, 1983; Ulf-Møller, 1998; Wasson et al., 2007) and by sub-solidus diffusion of Cr at much lower temperatures when metal solidification is complete (Kracher et al., 1977; Wasson et al., 1999). This suggests that the variable $D_{\text{chr-met}}$ and $\alpha_{\text{chr-met}}$ values, which are inferred by the modeling (Table 3), can be related to conditions that varied between the (ideal) endmember cases of (i) equilibrium partitioning and isotope fractionation of Zn at high temperature and (ii) diffusion-limited Zn partitioning and kinetic isotope fractionation at sub-solidus conditions.

The data of Fig. 5 require that the highest $D_{\text{chr-met}}$ values of 2800 and 3500 (for IAB complex and IIAB/IIIAB irons, respectively) are coupled with the smallest fractionations $\Delta^{66}\text{Zn}_{\text{chr-met}}$ (of $\sim 1.5\text{‰}$) and vice versa, for all three groups. This finding is in agreement with expectations as (i) (near-)equilibrium partitioning of Zn during fractional crystallization of chromite is likely to be associated with higher effective values of $D_{\text{chr-met}}$ than sub-solidus conditions, because slow Cr diffusion at low temperature may hinder attainment of full equilibrium partitioning and (ii) the isotope effects generated in equilibrium systems are typically smaller than kinetic isotope fractionations (Criss, 1999).

Unfortunately, only few independent constraints are available to verify the chosen values of $D_{\text{chr-met}}$ and $\alpha_{\text{chr-met}}$. Assuming equilibrium, the Zn concentrations for chromites in IAB irons (of up to $\sim 1.8\%$; Bunch et al., 1970; Kracher, 1985) and residual IAB Zn metal concentrations of as low as ~ 10 $\mu\text{g/g}$ (Fig. 3) are indicative of $D_{\text{chr-met}}$ values of up to 1800, in general agreement with the best fit $D_{\text{chr-met}}$ values inferred from the modeling (Table 3). Additional constraints are in accord with our inferred kinetic isotope fractionation factor of $\alpha_{\text{chr-met-kin}} \approx 0.9977$ to 0.9983. Whilst no published data are available for Zn isotope fractionation during diffusion in Fe–Ni melt, available results for diffusion of Zn in liquid Ag and Cd indicate that $\alpha_{\text{chr-met-kin}}$ is unlikely to be smaller than $\alpha = (m_{64}/m_{66})^{0.3} \approx 0.991$, and most probably larger than $\alpha = (m_{64}/m_{66})^{0.2} \approx 0.994$ (Richter et al., 2009).

3.5. Evaluation of the chromite segregation model

With the parameters of Table 3, best-fit chromite segregation models can be developed that produce excellent fits to the ob-

Table 3Parameters of the chromite segregation models that were used to account for the distinct $\delta^{66}\text{Zn}$, Zn and Cr systematics of the three iron meteorites groups.

		IAB complex	IIAB	IIIAB
Cr content of initial metal ($\mu\text{g/g}$)	$[\text{Cr}]_{\text{met-0}}$	300	350	350
Zn content of initial metal ($\mu\text{g/g}$)	$[\text{Zn}]_{\text{met-0}}$	55	0.5	6
$\delta^{66}\text{Zn}$ of initial metal	$\delta^{66}\text{Zn}_{\text{met-0}}$	+0.25‰	-0.25‰	-1.0‰
Chromite–metal partition coefficient for Zn	$D_{\text{chr-met}}$	550–2800	700–3500	550–3500
Chromite–metal fractionation factor for Zn ^a	$\alpha_{\text{chr-met}}$	0.9977–0.9985	0.9981–0.9985	0.9983–0.9986
Chromite–metal fractionation for Zn ^b	$\Delta^{66}\text{Zn}_{\text{chr-met}}$	-2.3 to -1.5‰	-1.9 to -1.5‰	-1.7 to -1.4‰
Following fractionation to $[\text{Cr}] = 5 \mu\text{g/g}$				
Mass fraction of fractionated chromite ^c	F_{chr}	0.64%	0.74%	0.74%
Mean final Zn content of chromite	$[\text{Zn}]_{\text{chr-f}}$	2.6–7.2%	0.02–0.06%	0.27–0.75%
Mean final $\delta^{66}\text{Zn}$ of chromite	$\delta^{66}\text{Zn}_{\text{chr-f}}$	-1.7 to -0.3‰	-1.7 to -0.6‰	-2.4 to -1.3‰

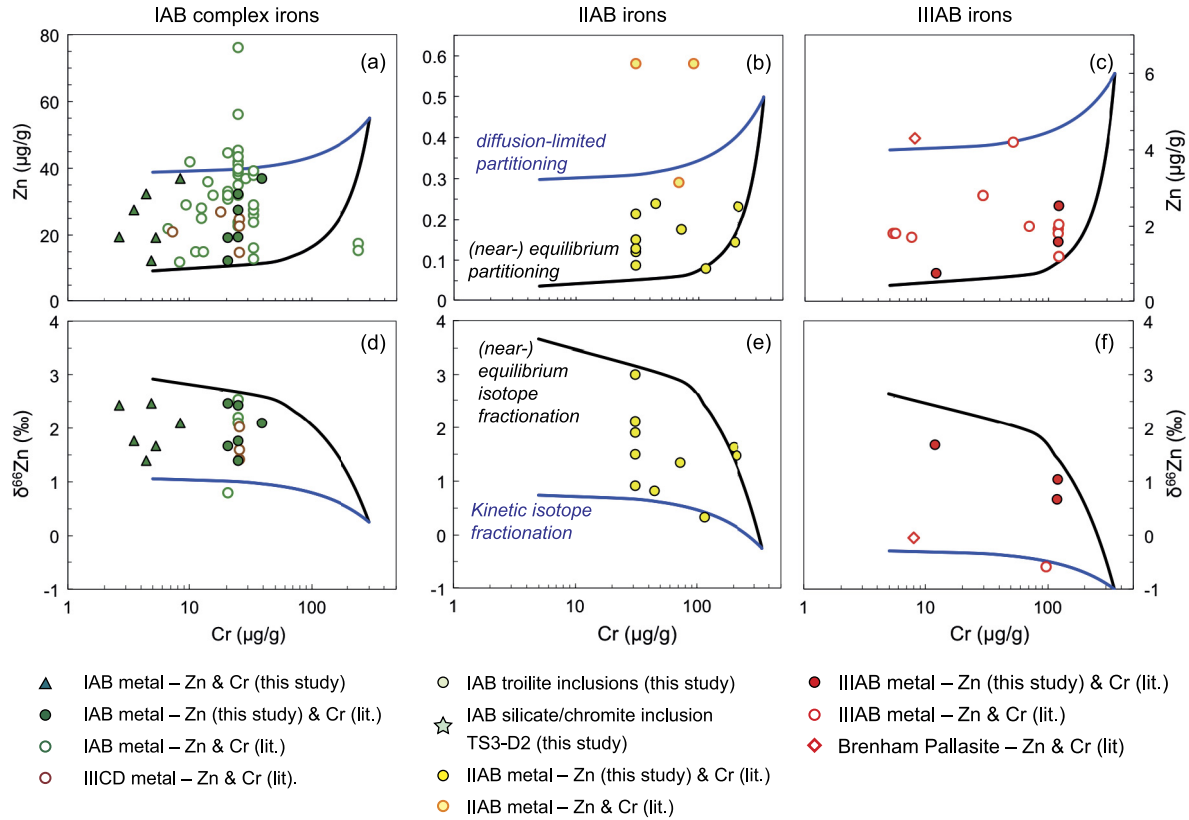
^a The chromite–metal isotope fractionation factor $\alpha_{\text{chr-met}}$ applies to the $^{66}\text{Zn}/^{64}\text{Zn}$ isotope ratio.^b $\Delta^{66}\text{Zn}_{\text{chr-met}}$ denotes the difference in isotopic composition between chromite and coexisting metal, as a result of isotope fractionation, such that $\Delta^{66}\text{Zn}_{\text{chr-met}} = \delta^{66}\text{Zn}_{\text{chr}} - \delta^{66}\text{Zn}_{\text{met}}$.^c F_{chr} denotes the mass fraction of chromite (in ‰), which must be extracted from the metal to account for the variable $\delta^{66}\text{Zn}$ values of the metal samples that fall on the calculated trends of Fig. 3.

Fig. 5. Plots of Zn, $\delta^{66}\text{Zn}$ and Cr concentrations for the samples analyzed in this study and iron meteorite data from the literature (lit). Also shown are the results of the chromite segregation model (Table 3), with the two endmember cases of (1) equilibrium partitioning and isotope fractionation of Zn (characterized by high $D_{\text{chr-met}}$ and small $\Delta^{66}\text{Zn}_{\text{chr-met}} \approx -1.4$ to -1.5 ‰; black lines) and (2) diffusion-limited partitioning and kinetic isotope fractionation for Zn (with low $D_{\text{chr-met}}$ and larger $\Delta^{66}\text{Zn}_{\text{chr-met}} \approx -1.7$ to -2.3 ‰; blue lines). Using very similar parameters for all three groups, the chromite segregation model accounts well for the observed data trends. See supplementary Tables S4, S5 for details and sources of the coupled Zn–Cr and $\delta^{66}\text{Zn}$ –Cr data. Uncertainties are not shown for simplicity and the data for Casas Grandes IIIAB, with an anomalously high Zn content of $10.9 \mu\text{g/g}$ (Luck et al., 2005) that may reflect contamination, is omitted from panels (c) and (f). (For interpretation of the references to color in this figure, the reader is referred to the web version of this article.)

served Zn– $\delta^{66}\text{Zn}$ –Cr systematics (Figs. 4, 5) using reasonable and consistent values for all variables. Here, we evaluate whether these best-fit models are robust with respect to alternative solutions and different interpretations of the trends.

Mixing offers a possible alternative explanation for the observed $\delta^{66}\text{Zn}$ vs. Zn trends of the three iron groups, if this involves chromite characterized by high Zn in conjunction with $\delta^{66}\text{Zn} \approx 0$ to -1 and a metal phase with low Zn content and high $\delta^{66}\text{Zn}$ (Fig. 6). Such endmember compositions, however, are most reasonably produced by chromite formation and partitioning of Zn into this phase. The Zn data of this study and most previous investiga-

tions (Figs. 3, 4) were, furthermore, acquired using solution-based methods that do not sample chromite-sited Zn, or only to a minor extent. This indicates that partitioning of Zn into chromite and associated isotope fractionation provides the most straightforward explanation for the Zn– $\delta^{66}\text{Zn}$ –Cr systematics of irons whilst mixing likely played only a secondary role in setting the observed relationships. This is an important conclusion, because it implies that the bulk metal will be similar in composition to the initial metal, as inferred by the chromite segregation model (Table 3).

The best fits of the chromite segregation model to the data of the three iron groups are obtained for metal phases with similar

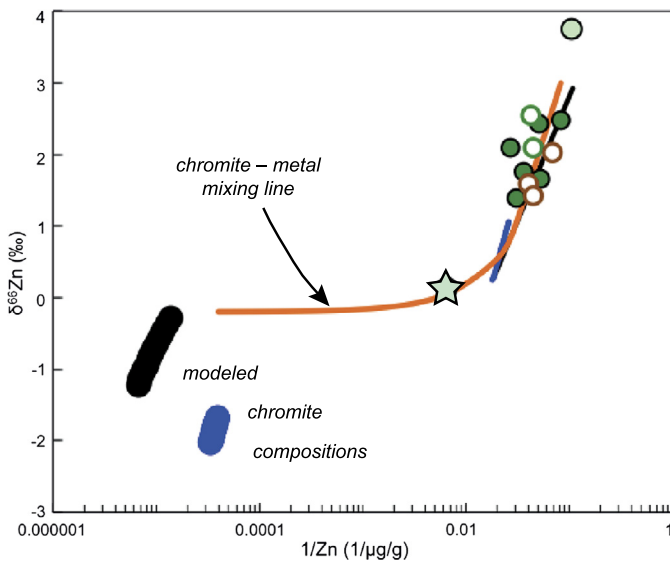


Fig. 6. Plot of $\delta^{66}\text{Zn}$ vs. $1/\text{Zn}$ concentration for samples of IAB complex irons (symbols as Fig. 4). Also shown are (1) the range of metal (thin lines) and chromite (thick lines) compositions inferred by the chromite segregation model (Table 3) for IAB complex irons based on the 'equilibrium' and the 'kinetic' endmember scenarios (black and blue lines respectively), and (2) a hypothetical mixing line (brown) between a chromite (2.5% Zn and $\delta^{66}\text{Zn} = -0.2\text{‰}$) and a metal (12 $\mu\text{g/g}$ Zn and $\delta^{66}\text{Zn} = +3\text{‰}$). Such mixing can explain the observed $\delta^{66}\text{Zn}$ vs. $1/[\text{Zn}]$ correlations of the metal samples (Fig. 4) but is unlikely to be primarily responsible for the data trends (see text). The silicate–chromite inclusion TS3-D2 lies on the inferred mixing trend, with a Zn isotope composition akin to the 'calculated' chromites but at a much lower Zn content. This is expected because the Zn concentration of TS3-D2 is diluted by the presence of silicates. Literature data and sources are compiled in supplementary Table S3; uncertainties are not shown for simplicity. (For interpretation of the references to color in this figure, the reader is referred to the web version of this article.)

initial Zn isotope compositions of $\delta^{66}\text{Zn}_{\text{met-0}} = -1\text{‰}$ to $+0.25\text{‰}$. Furthermore, the initial Zn concentrations $[\text{Zn}]_{\text{met-0}}$ inferred by the models clearly reflect the distinct Zn concentrations that are observed for the different groups, such that $[\text{Zn}]_{\text{met-0}}$ decreases from 55 $\mu\text{g/g}$ for the IAB complex irons, to 6 $\mu\text{g/g}$ for IIIABs and 0.5 $\mu\text{g/g}$ for IIABs (Table 3). Importantly, these model results are robust over a reasonable range of parameter space.

Alternative models, which apply higher and lower values of $\delta^{66}\text{Zn}_{\text{met-0}}$, for example of $+2\text{‰}$ and -2‰ , are feasible in principle but require that the isotope fractionation $\Delta^{66}\text{Zn}_{\text{chr-met}}$ is either $\sim 0\text{‰}$ or less than -4‰ , respectively. Such fractionations, however, would produce average final chromite compositions $\delta^{66}\text{Zn}_{\text{chr-f}}$ of about $+2\text{‰}$ and less than -2‰ . In contrast, the chromite-rich sample TS3-D2 features $\delta^{66}\text{Zn} \approx +0.1\text{‰}$, in support of the models summarized in Table 3. Similarly, changes in the relative order of the concentrations $[\text{Zn}]_{\text{met-0}}$ for the three groups of irons can be accommodated but only with $D_{\text{chr-met}}$ values, which show large variances between groups. As an example, $[\text{Zn}]_{\text{met-0-IIAB}} \approx [\text{Zn}]_{\text{met-0-IIIAB}} \approx 3 \mu\text{g/g}$ can be achieved for $D_{\text{chr-met-IIAB}} \approx 4000\text{--}6000$ and $D_{\text{chr-met-IIIAB}} \approx 600\text{--}3000$. This stands in contrast to our preferred result, which reasonably features similar $D_{\text{chr-met}}$ values throughout (Table 3). Furthermore, our preferred choice of parameters can reproduce the observed variability in $[\text{Zn}]$ and $\delta^{66}\text{Zn}$ (Figs. 3, 4) with formation of only minor amounts of chromite ($<1\text{‰}$ of metal mass; Table 3), in general accord with observations on the abundance of chromite in iron meteorites (e.g., Bunch et al., 1970; Buchwald, 1977). It was also proposed, however, that chromite could rise during core formation due to density contrasts and separate from the metal, such that chromite abundance estimates may generally be too low (Chabot et al., 2009).

Previous studies reported ZnO contents of 1.1 to 2.2% for chromites from seven IAB irons, whereas significantly lower ZnO concentrations of between 0.15 and 0.34% were found in chromites of the IIIAB irons Cape York and Bagdad (supplementary Table S6). These observations are also in good agreement with our model because this predicts an order of magnitude difference in the Zn contents of chromites from IAB complex and IIIAB irons (Table 3). The high final Zn concentration of chromite $[\text{Zn}]_{\text{chr-f}}$ inferred by the IAB model (2.6 to 7.2%, Table 3), however, clearly exceeds the range of Zn contents observed for IAB chromites. It is possible that this discrepancy reflects sequestration of Zn into other accessory phases in specific cases (e.g., sphalerite; Kracher et al., 1977), sample heterogeneity and/or the small population of chromites analyzed to date. Notably, higher ZnO contents of $>3\%$ were reported for the ungrouped S-rich meteorite Soroti (Kracher et al., 1998). Furthermore, the measured Zn/Cr ratio of ~ 0.24 for the silicate–chromite sample TS3-D2 (Table 1) translates into a Zn concentration of about 10%, potentially indicative of a very Zn-rich chromite. The latter data must be considered with caution, however, because it is possible that the high Zn/Cr reflects partial dissolution of a chromite-rich mineral mixture, whereby the digestion released most of the Zn but only part of the Cr inventory.

In summary, the modeling demonstrates that the observed variations in $\delta^{66}\text{Zn}$ and Zn contents for the three iron meteorite groups (Fig. 3) can be accounted for by preferential partitioning of isotopically light Zn into chromite at conditions that are inferred to have varied from (near-)equilibrium partitioning between solid chromite and Fe–Ni melt to sub-solidus diffusion of Zn into chromite grains. Significantly, the model indicates that the initial (and therefore the bulk) metal compositions were characterized by Zn contents that decreased in the order IAB complex $>$ IIIAB $>$ IIAB irons but featured similar Zn isotope compositions of $\delta^{66}\text{Zn} \approx 0$ throughout.

3.6. Comparative Zn isotope systematics of iron meteorites, chondrites and the bulk silicate Earth

In the following, the inferred bulk metal $\delta^{66}\text{Zn}$ values of the three iron meteorite groups are compared with Zn isotope data for the Earth and chondritic meteorites. Whilst there are numerous Zn isotope studies of terrestrial samples only few data are available for the mantle-derived basalts and peridotites, which are best suited for characterizing the composition of the bulk silicate Earth (BSE). This small mantle dataset (supplementary Table S7) reveals a limited range in $\delta^{66}\text{Zn}$ values from -0.10‰ to $+0.48\text{‰}$, such that the BSE is likely characterized by $\delta^{66}\text{Zn} = +0.25 \pm 0.25\text{‰}$ (Fig. 2b; supplementary Table S7). Given the conclusions that (i) Zn isotope fractionation during core segregation was probably small or negligible and (ii) only a minor fraction of the Earth's Zn budget resides in the core because Zn is largely lithophile (with $D_{\text{met-sil}} < 1$; Table 2; Corgne et al., 2008; Lagos et al., 2008; Mann et al., 2009), it is reasonable to assume that the bulk Earth and the BSE have nearly identical $\delta^{66}\text{Zn}$.

Published data for chondritic meteorites indicate that they are derived from parent bodies with similar Zn isotope compositions (Fig. 2b; supplementary Table S8). Based on the current literature, carbonaceous and ordinary chondrites feature $\delta^{66}\text{Zn}$ values of $+0.1$ to $+0.5\text{‰}$ and -1.3 to $+0.4\text{‰}$, respectively, whereby the slightly larger isotopic variability of the latter samples probably reflects isotope fractionation from Zn mobilization during parent body metamorphism, as inferred for Cd (Wombacher et al., 2008). An even larger variability of $\delta^{66}\text{Zn}$ is shown by enstatite chondrites ($\delta^{66}\text{Zn} \approx 0$ to $+7.4\text{‰}$) but this presumably also reflects Zn redistribution by secondary processes (Moynier et al., 2011).

In contrast to terrestrial rocks and most chondrites, the metal samples of IAB complex, IIAB and IIIAB irons display distinctly higher $\delta^{66}\text{Zn}$ values and more isotopic variability (Fig. 2b). These

characteristics are, however, most likely the result of chromite segregation and Zn partitioning into this phase. An important conclusion of our work is that the iron meteorite parent bodies featured bulk metal compositions of $\delta^{66}\text{Zn} \approx 0$. Given the additional evidence that metal–silicate differentiation was not associated with significant Zn isotope fractionation, the data suggest that the iron meteorite parent bodies were also characterized by $\delta^{66}\text{Zn} \approx 0 \pm 1\%$. Our new results thus indicate that the Earth and the parent bodies of chondritic and iron meteorites may all have had similar Zn isotope compositions despite large differences in bulk Zn contents. This reinforces earlier work (e.g., Humayun and Clayton, 1995; Wombacher et al., 2008), which showed that the processes responsible for the formation of variably volatile depleted matter in the early solar nebula did not generate significant stable isotope effects.

4. Conclusions

Three metal–silicate partitioning experiments were conducted in MgO capsules at 1.5 GPa and 1650 K for 10 to 60 min. The experiments demonstrate that Zn has a slight preference for silicate melts (with $D_{\text{met-sil}} \approx 0.7$), in agreement with previous studies, and indicate that Zn isotope fractionation between molten metal and silicate is either small or absent. The latter finding is not only directly relevant for meteorite parent bodies but also most likely applicable to the Earth.

Our new and previously published data show that metal samples of IAB complex, IIAB and IIIAB iron meteorites display distinct ranges in Zn contents and feature positive but essentially identical $\delta^{66}\text{Zn}$ values. Samples from each iron meteorite group furthermore define distinct linear correlations of $\delta^{66}\text{Zn}$ with $1/\text{Zn}$. Based on the low $\delta^{66}\text{Zn}$ value determined for a chromite-rich inclusion of Toluca and modeling, these trends are thought to reflect segregation of minor amounts of Zn-rich chromite from iron meteorite metals and associated isotope fractionation with $\Delta^{66}\text{Zn}_{\text{chr-met}} \approx -1.5\%$. This process produces residual Zn-depleted metal samples characterized by high $\delta^{66}\text{Zn}$, in accord with the analytical results.

Taken together, our findings suggest that the parent bodies of IAB complex, IIAB and IIIAB iron meteorites were characterized by $\delta^{66}\text{Zn}$ values of about $0 \pm 1\%$, essentially indistinguishable from the Zn isotope composition of the BSE and similar to data obtained for carbonaceous and ordinary chondrites. Hence, most solar system bodies appear to be characterized by similar bulk Zn isotope compositions, despite large differences in Zn contents.

Acknowledgements

Katharina Kreissig and the other members of the MAGIC team are thanked for their support in keeping the mass spec running and the clean lab organized. M. Humayun provided helpful tips in a discussion of our Zn data whilst contributions by A. Kracher were of immense help in gaining a better understanding of chromites in iron meteorites. The critical and constructive comments of two anonymous referees and editor Tim Elliott played a key role in shaping a significantly improved revised version of this article. Graeme Poole and Carl Palk provided helpful tips to improve wording of the discussion. The research was supported by STFC grants to MR, GB and MS.

Appendix A. Supplementary material

Supplementary material related to this article can be found online at <http://dx.doi.org/10.1016/j.epsl.2014.05.029>.

References

- Andreasen, R., Rehkämper, M., Benedix, G.K., Theis, K., Schönbächler, M., Smith, C., 2012. Pb–Tl chronology of IIAB and IIIAB iron meteorites. *Mineral. Mag.* 76, 1426.
- Arnold, T., Schönbächler, M., Rehkämper, M., Dong, S., Zhao, F.-J., Kirk, G.J.D., Coles, B.J., Weiss, D.J., 2010. Determination of zinc stable isotope compositions in geological and biological samples by double spike MC-ICPMS. *Anal. Bioanal. Chem.* 398, 3115–3125.
- Benedix, G.K., McCoy, T.J., Keil, K., Love, S.G., 2000. A petrographic study of the IAB iron meteorites: constraints on the formation of the IAB-wononaite parent body. *Meteorit. Planet. Sci.* 35, 1127–1141.
- Benedix, G.K., Haack, H., McCoy, T.J., 2013. Iron and stony-iron meteorites. In: Davis, A.M. (Ed.), *Meteorites, Comets, and Planets*. 2nd ed. Elsevier, Amsterdam, pp. 325–345.
- Buchwald, V.F., 1977. Mineralogy of iron meteorites. *Philos. Trans. R. Soc. Lond. A* 286, 453–491.
- Bunch, T.E., Keil, K., Olsen, E., 1970. Mineralogy and petrology of silicate inclusions in iron meteorites. *Contrib. Mineral. Petrol.* 25, 297–340.
- Chabot, N.L., Haack, H., 2006. Evolution of asteroidal cores. In: Lauretta, D.S., McSween Jr., H.Y. (Eds.), *Meteorites and the Early Solar System II*. University of Arizona Press, Tucson, pp. 747–771.
- Chabot, N.L., Saslow, S.A., McDonough, W.F., Jones, J.H., 2009. An investigation of the behavior of Cu and Cr during iron meteorite crystallization. *Meteorit. Planet. Sci.* 44, 505–519.
- Choi, B.G., Ouyang, X.W., Wasson, J.T., 1995. Classification and origin of IAB and IIIAB iron meteorites. *Geochim. Cosmochim. Acta* 59, 593–612.
- Corgne, A., Keshav, S., Wood, B.J., McDonough, W.F., Fei, Y.W., 2008. Metal–silicate partitioning and constraints on core composition and oxygen fugacity during Earth accretion. *Geochim. Cosmochim. Acta* 72, 574–589.
- Criss, R.E., 1999. *Principles of Stable Isotope Distribution*. Oxford University Press, Oxford.
- Ghidani, O.Y., Loss, R.D., 2011. Isotope fractionation and concentration measurements of Zn in meteorites determined by the double spike, IDMS-TIMS techniques. *Meteorit. Planet. Sci.* 46, 830–842.
- Göpel, C., Manhès, G., Allègre, C.J., 1985. U–Pb systematics in iron meteorites: uniformity of primordial lead. *Geochim. Cosmochim. Acta* 49, 1681–1695.
- Haack, H., McCoy, T.J., 2003. Iron and stony-iron meteorites. In: Davis, A.M. (Ed.), *Meteorites, Comets, and Planets*. Elsevier, Amsterdam, pp. 325–345.
- Humayun, M., Clayton, R.N., 1995. Potassium isotope cosmochemistry: genetic implications of volatile element depletion. *Geochim. Cosmochim. Acta* 59, 2131–2148.
- Jochum, K.P., Nohl, U., Herwig, K., Lammel, E., Stoll, B., Hofmann, A.W., 2005. GeoReM: a new geochemical database for reference materials and isotopic standards. *Geostand. Geoanal. Res.* 29, 333–338.
- Kehm, K., Hauri, E.H., Alexander, C.M.O.D., Carlsen, R.W., 2003. High precision iron isotope measurements of meteoritic material by cold plasma ICP-MS. *Geochim. Cosmochim. Acta* 67, 2879–2891.
- Kohn, S.C., Schofield, P.F., 1994. The importance of melt composition in controlling trace-element behaviour: an experimental study of Mn and Zn partitioning between forsterite and silicate melts. *Chem. Geol.* 117, 73–87.
- Kracher, A., 1983. Notes on the evolution of the IIIAB/pallasite parent body. *Lunar Planet. Sci. Conf. XIV*, 405–406.
- Kracher, A., 1985. The evolution of partially differentiated planetesimals – evidence from iron meteorite groups IAB and IIIAB. *J. Geophys. Res.* 90 (Supplement), C689–C698.
- Kracher, A., Kurat, G., Buchwald, V.F., 1977. Cape-York: the extraordinary mineralogy of an ordinary iron meteorite and its implication for the genesis of IIIAB irons. *Geochem. J.* 11, 207–217.
- Kracher, A., Gramstad, S.D., Kurat, G., 1998. Soroti and the origin of sulfide-rich meteorites. *Meteorit. Planet. Sci.* 33 (Supplement), A88–A89.
- Lagos, M., Ballhaus, C., Münker, C., Wohlgemuth-Ueberwasser, C., Berndt, J., Kuzmin, D., 2008. The Earth's missing lead may not be in the core. *Nature* 456, 89–92.
- Larner, F., Rehkämper, M., 2012. Evaluation of stable isotope tracing for ZnO nanomaterials – new constraints from high precision isotope analyses and modeling. *Environ. Sci. Technol.* 46, 4149–4158.
- Luck, J.-M., Ben Othman, D., Albarède, F., 2005. Zn and Cu isotopic variations in chondrites and iron meteorites: early solar nebula reservoirs and parent-body processes. *Geochim. Cosmochim. Acta* 69, 5351–5363.
- Mann, U., Frost, D.J., Rubie, D.C., 2009. Evidence for high-pressure core–mantle differentiation from the metal–silicate partitioning of lithophile and weakly-siderophile elements. *Geochim. Cosmochim. Acta* 73, 7360–7386.
- Maréchal, C.N., Télouk, P., Albarède, F., 1999. Precise analysis of copper and zinc isotopic compositions by plasma-source mass spectrometry. *Chem. Geol.* 156, 251–273.
- McCoy, T.J., Mittlefehldt, D.W., Wilson, L., 2006. Asteroid differentiation. In: Lauretta, D.S., McSween Jr., H.Y. (Eds.), *Meteorites and the Early Solar System II*. University of Arizona Press, Tucson, pp. 733–745.
- Mittlefehldt, D.W., McCoy, T.J., Goodrich, C.A., Kracher, A., 1998. Non-chondritic meteorites from asteroidal bodies. In: Papike, J.J. (Ed.), *Planetary Materials*. Mineralogical Society of America, Washington, DC, pp. 4-01–4-195.

- Moynier, F., Rushmer, T., Albarède, F., 2005. Zn isotopic mass fractionation during high temperature segregation of metal from silicate. In: 68th Annual Meteoritical Society Meeting, p. 5223.
- Moynier, F., Blichert-Toft, J., Télouk, P., Luck, J.-M., Albarède, F., 2007. Comparative stable isotope geochemistry of Ni, Cu, Zn, and Fe in chondrites and iron meteorites. *Geochim. Cosmochim. Acta* 71, 4365–4379.
- Moynier, F., Paniello, R.C., Gounelle, M., Albarède, F., Beck, P., Podosek, F., Zanda, B., 2011. Nature of volatile depletion and genetic relationships in enstatite chondrites and aubrites inferred from Zn isotopes. *Geochim. Cosmochim. Acta* 75, 297–307.
- Nielsen, S.G., Rehkämper, M., Halliday, A.N., 2006. Thallium isotopic variations in iron meteorites and evidence for live lead-205 in the early solar system. *Geochim. Cosmochim. Acta* 70, 2643–2657.
- Presnall, D.C., Dixon, S.A., Dixon, J.R., Odonnell, T.H., Brenner, N.L., Schrock, R.L., Dycus, D.W., 1978. Liquidus phase relations on join diopside–forsterite–anorthite from 1 atm to 20 kbar – their bearing on generation and crystallization of basaltic magma. *Contrib. Mineral. Petrol.* 66, 203–220.
- Richter, F.M., Dauphas, N., Teng, F.-Z., 2009. Non-traditional fractionation of non-traditional isotopes: evaporation, chemical diffusion and Soret diffusion. *Chem. Geol.* 258, 92–103.
- Schulz, T., Münker, C., Palme, H., Mezger, K., 2009. Hf–W chronometry of the IAB iron meteorite parent body. *Earth Planet. Sci. Lett.* 280, 185–193.
- Scott, E.R.D., 1972. Chemical fractionation in iron meteorites and its interpretation. *Geochim. Cosmochim. Acta* 36, 1205–1236.
- Scott, E.R.D., 1977. Geochemical relationships between some pallasites and iron meteorites. *Mineral. Mag.* 41, 265–272.
- Theis, K.J., Schönbächler, M., Benedix, G.K., Rehkämper, M., Andreasen, R., Davies, C., 2013. Palladium–silver chronology of IAB iron meteorites. *Earth Planet. Sci. Lett.* 361, 402–411.
- Ulf-Møller, F., 1998. Effects of liquid immiscibility on trace element fractionation in magmatic iron meteorites: a case study of group IIIAB. *Meteorit. Planet. Sci.* 33, 207–220.
- Wasson, J.T., 1999. Trapped melt in IIIAB irons; solid/liquid elemental partitioning during the fractionation of the IIIAB magma. *Geochim. Cosmochim. Acta* 63, 2875–2889.
- Wasson, J.T., Kallemeyn, G.W., 2002. The IAB iron-meteorite complex: a group, five subgroups, numerous grouplets, closely related, mainly formed by crystal segregation in rapidly cooling melts. *Geochim. Cosmochim. Acta* 66, 2445–2473.
- Wasson, J.T., Lange, D.E., Francis, C.A., Ulf-Møller, F., 1999. Massive chromite in the Brenham pallasite and the fractionation of Cr during the crystallization of asteroidal cores. *Geochim. Cosmochim. Acta* 63, 1219–1232.
- Wasson, J.T., Huber, H., Malvin, D.J., 2007. Formation of IAB iron meteorites. *Geochim. Cosmochim. Acta* 71, 760–781.
- Wombacher, F., Rehkämper, M., Mezger, K., Bischoff, A., Münker, C., 2008. Cadmium stable isotope cosmochemistry. *Geochim. Cosmochim. Acta* 72, 646–667.
- Zhu, X.K., Guo, Y., O’Nions, R.K., Young, E.D., Ash, R.D., 2001. Isotopic homogeneity of iron in the early solar system. *Nature* 412, 311–313.